

New approach for filling simulations of dual-scale preforms using BEM for the manufacturing of composites materials

Nuevo enfoque para simulaciones de llenado de preformas doble escala usando BEM para la manufactura de compuestos

Iván David Patiño Arcila ¹

¹Grupo de Investigación e Innovación Ambiental (GIIAM), Facultad de Ingeniería, Institución Universitaria Pascual Bravo. Calle 54A # 30-01. C. P. 050034. Medellín, Colombia.



CITE THIS ARTICLE AS:

I. D. Patiño-Arcila. "New approach for filling simulations of dual-scale preforms using BEM for the manufacturing of composites materials", *Revista Facultad de Ingeniería Universidad de Antioquia*, no. 107, pp. 66-79, Apr-Jun 2023. [Online]. Available: <https://www.doi.org/10.17533/udea.redin.20220783>

ARTICLE INFO:

Received: November 16, 2021
Accepted: July 01, 2022
Available online: July 05, 2022

KEYWORDS:

Fibrous reinforcements; liquid composite molding; multi-scale filling; boundary elements; polymers

Refuerzos fibrosos; moldeo líquido de compuestos; llenado multi-escala; elementos de frontera; polímeros

ABSTRACT: Some reinforcements used in the manufacturing of composites parts by Liquid Composite Molding (LCM) processes have a dual-scale nature, which supposes flow imbalances between the tows and channels at the mesoscopic scale, which in turn, cause uncontrolled defects (voids, dry points, among others) and could considerably affect the global flow behavior during the filling of cavities at a macroscopic scale. In the present work, a new approach to conducting filling simulations of dual-scale fibrous reinforcements at a mesoscopic scale is proposed. This consists of imposing a pressure gradient across the Representative Unitary Cell, and considering Stokes-Darcy coupling conditions between the porous and the free-fluid sub-domains to determine the filling of the former ones. Contrarily to the traditional approach, where a uniform pressure is assumed for the channels, and only the porous media fluid is modeled, the present approach allows considering the fluid motion at channels, flow-direction dependent capillary pressure, air compression and dissolution, and vacuum pressure, as well as capturing several phenomena of the evolution of intra-tow bubbles, namely, compression, mobilization at constant volume and migration from tows towards the channel. The velocity vectors and streamlines in the tows and channel subdomains, when these phenomena take place, are analyzed as well.

RESUMEN: Algunos refuerzos usados en la fabricación de piezas por Procesos de Moldeo Líquido (LCM) tienen una naturaleza de doble-escala, lo cual supone desbalances de flujo entre las mechas y canales a escala mesoscópica, lo cual a su vez, causa defectos no controlados (vacíos, puntos secos, entre otros) y puede afectar considerablemente el comportamiento global del flujo durante el llenado de cavidades a escala macroscópica. En el presente trabajo, un nuevo enfoque para llevar a cabo simulaciones de llenado de refuerzos fibrosos de doble escala a nivel mesoscópico es propuesto. Éste consiste en imponer un gradiente de presión a lo largo de la Celda Representativa Unitaria, y condiciones de acople Stokes-Darcy entre los subdominios porosos y de fluido libre para determinar el llenado de los primeros. Contrariamente al enfoque tradicional, donde una presión uniforme es asumida en los canales y sólo el fluido en los medios porosos es modelado, el presente enfoque permite considerar el movimiento de fluido en los canales, presión capilar dependiente de la orientación, compresión y disolución del aire, y presión de vacío, de igual manera que capturar diferentes fenómenos de la evolución de vacíos intra-mechas: compresión, movilización a volumen constante y migración desde las mechas hacia el canal. Los vectores de velocidad y líneas de corriente en los subdominios mechas y canal, cuando estos fenómenos tienen lugar, son analizados también.

* Corresponding author: Iván David Patiño Arcila

E-mail: ivandavidpatino@gmail.com

ISSN 0120-6230

e-ISSN 2422-2844



Nomenclature table

L_{RUC}	Length of Representative Unitary Cell	μ	Fluid viscosity
H_{RUC}	Height of Representative Unitary Cell	R_f	Fiber radius
H_g	Height of channel	V_f	Fiber volume fraction
P_{in}	Inlet pressure	\hat{n}_i	Normal vector outwardly oriented from the Stokes domain
P_{out}	Outlet pressure	s	Index standing for Stokes
P_{ff}	Pressure of fluid front	d	Index standing for Darcy
P_{air}	Air pressure	γ	Slip coefficient
P_{cap}	Capillary pressure	$\hat{\tau}_i$	Tangential vector at the Stokes-Darcy interface
a_1	Major semi-axis of weft	K	Permeability tensor
a_2	Minor semi-axis of weft	ε_t	Tow porosity
u_i	Component "i" of velocity field	$\sigma_{ij}^{(s)}$	Cauchy stress tensor in the Stokes domain
P	Fluid pressure in the channel	$p^{(d)}$	Pressure in the Darcy domain
$\langle u_f \rangle_i$	Component "i" of volume-averaged velocity	t_1^{inl}	Inlet surface tractions in the horizontal direction
$\langle P_f \rangle^f$	Pressure in the porous sub-domain (tow)	t_1^{out}	Outlet surface tractions in the horizontal direction
K_i	Component "i" of anisotropic permeability	$\overline{p_{tnl}}$	Prescribed inlet pressure
u_n	Normal velocity of the moving boundary	$\overline{p_{out}}$	Prescribed outlet pressure
σ	Surface tension of liquid	u_2^{inl}	Inlet vertical velocity
κ	Curvature of the liquid-air interface	u_2^{out}	Outlet vertical velocity
$A_{int,s}$	Cross-sectional area of the solid particles in the flow direction	φ	Angle between direction of the moving fluid front and the fiber axis.
C_{int}	Wetted perimeter of the solid particles	n_f	Number of fibers inside the tows
L_f	Length of fibers	η	Relative spacing ratio
d	Half-distance between fibers	θ	Contact angle
α	Solid angle at the source point	ξ	Source points in the original coordinate system
$u_j(y)$	Component "j" of velocity in the field point y	y	Field points in the original coordinate system
$t_j(y)$	Component "j" of traction in the field point y	ξ^e	Source points in the EIS system
$p(y^e)$	Pressure in the field point y^e of EIS system	y^e	Field points in the EIS system
$q(y^e)$	Pressure flux in the field point y^e of EIS system	r	Euclidean distance between source and field point
h_s	Height of the Stokes sub-domain	r^e	Euclidean distance between source and field point in the EIS space
h_d	Height of the Darcy sub-domain	u_x	Horizontal velocity
u_1^-	Velocity at the Stokes-Darcy interface (in the Stokes Domain)	u_y	Vertical velocity
l	Length of domain of analytical solution	$C_{int,s}$	Wetted perimeter of the solid particles in the flow direction
$A_{int,s}$	Cross-sectional area of the solid particles in the flow direction	μ_{air}	Air viscosity at 25 °C

1. Introduction

A porous medium at the mesoscopic scale can be classified according to the different orders of permeability into single-scale and dual-scale porous medium. In a single-scale porous medium, there is only one scale of permeability in the Representative Unitary Cell (RUC); conversely, a dual-scale porous medium comprises two

scales of permeability, which can be very different from each other. In the field of composites processing, some fibrous reinforcements used in the manufacturing of parts by Liquid Composite Molding (LCM) behave as dual-scale porous media, which implies flow imbalances inside the RUC. In dual-scale fibrous reinforcements, there are three well-differentiated sub-domains at mesoscopic scale: channels, longitudinal tows and transverse tows, as

shown in Figure 1. The channel permeability is larger than such of the tows, which causes a non-uniform saturation of the fibrous reinforcement, which in turn can significantly influence the behavior of macroscopic variables during the mold filling.

The phenomenon of filling of dual-scale porous media can be divided into two coupled problems: the filling of a Representative Unit Cell (RUC) having a specific architecture and regions of different permeabilities (mesoscopic problem) [1–8], and the filling of cavities taking into account the effects produced by the imbalances of flow inside the RUC's (macroscopic problem) [3, 6, 9–12]. At the mesoscopic level, the uneven saturation of the fibrous reinforcement depends on the relationship between the viscous and capillary forces, and it can considerably affect the pressure and velocity fields at the macroscopic level.

The present work proposes a new approach for conducting filling simulations of dual-scale preforms at a mesoscopic scale. In the traditional approach, a uniform liquid pressure in the channels is supposed and the tow saturation phenomenon is governed by classical equations of porous media, such as Forchheimer, Brinkman, and Darcy, among others [10, 11, 13–20]. This approach entails some limitations: fluid flow motion at the channel is not considered since a uniform pressure is prescribed, air compressibility is not taken into account, capillary pressure is independent of the flow direction relative to the bank of fibers, and dynamic evolution of voids in the RUC is not fully captured. The approach proposed here consists of prescribing a pressure gradient along the RUC and imposing Stokes-Darcy matching conditions between the tows and the channel sub-domains to determine the filling of the former ones. This allows considering the fluid flow velocity at the channel sub-domain, while two additional phenomena of the dynamic of intra-tow bubbles are well reproduced: void mobilization at constant volume and migration from the weft towards the channel. Additionally, air compressibility is deemed, as well as a flow-direction-dependent capillary pressure. Therefore, the present approach mimics the real conditions of composites processing more closely.

It is important to highlight that in both the traditional and proposed approaches, the assumption of full filled channels is valid since the prescribed channel pressures are at least one order of magnitude larger than the calculated capillary pressures; this assumption is extensively used in applications of composite manufacturing using LCM, and is particularly useful to simplify the coupling between the mesoscopic and macroscopic scales. The main contributions of the present work can be summarized as follows:

- The presentation of the capabilities of a new approach to capturing several bubble phenomena at a mesoscopic scale during the filling of dual-scale fibrous reinforcement (compression, displacement and migration); these phenomena are neglected when using the traditional approach and have a direct influence on the pressure, velocity and saturation fields at a macroscopic scale. In future works, the present approach will allow including the effects of these phenomena on the macroscopic filling of dual-scale fibrous reinforcements.
- The calculation and analysis of the velocity vector field and streamlines during the stages of compression, displacement, and migration of the bubble formed inside the weft by mechanical entrapment of air. As shown later, these results are physically consistent with the assumption of full-filled channels and the matching conditions Stokes-Darcy used in the present work.

The present paper is organized as follows. In section 2, the mathematical models and numerical methods involved in the proposed approach are described. In section 3, the present Stokes-Darcy approach is validated with the analytical solution of a coupled free fluid/porous medium problem, and then, it is compared to the classical approach in terms of the saturation evolution in the warps and weft; additionally, the velocity fields and streamlines in the channel and tows sub-domains predicted by the present approach are analyzed. In Section 4, the principal conclusions and contributions of this work are addressed.

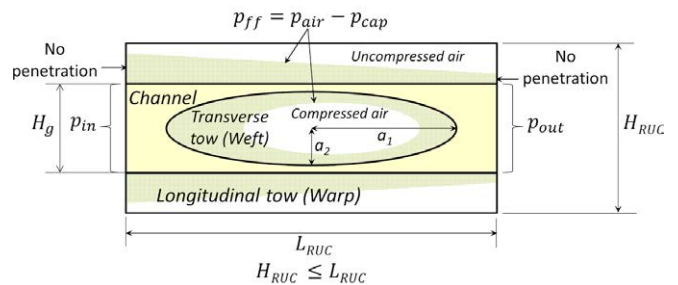


Figure 1 Shape and principal dimensions of the Representative Unitary Cell (RUC) of the dual-scale preform

2. Stokes-Darcy approach for filling simulation of dual-scale fibrous reinforcements

The present section summarizes the governing equations, boundary conditions, matching conditions, and numerical

techniques used to solve the mathematical model and track the fluid front are summarized. More details about this numerical implementation in dual-scale fibrous reinforcements can be found in [21].

2.1 Governing equations, boundary and matching conditions

When the Reynolds number of channels and the tows permeability are small, the coupling between the free-fluid and porous sub-domains depicted in Figure 1 can be defined by a Stokes-Darcy formulation as given by equations 1 to 4

For the channel (Stokes domain):

$$\mu (\partial^2 u_i / \partial x_j \partial x_j) - \partial p / \partial x_i = 0 \quad (1)$$

$$\partial u_i / \partial x_i = 0 \quad (2)$$

For the porous medium (Darcy flow in the principal directions of permeability):

$$\langle u_f \rangle_i = - (K_i / \mu) \cdot (\partial \langle p_f \rangle^f / \partial x_i) \quad (3)$$

$$\partial \langle u_f \rangle_i / \partial x_i = 0 \quad (4)$$

On the other hand, the architecture of the porous media (warps and weft) is considered as a bank of aligned micro-cylinders, and the main permeabilities can be computed using the model proposed by Gebart [22], equations 5, 6:

$$K_1 = 8R_f^2 \cdot (1 - V_f)^3 / (c \cdot (V_f)^2) \quad (5)$$

$$K_2 = c_1 \left(\sqrt{V_{f,\max} / V_f} - 1 \right)^{5/2} R_f^2 \quad (6)$$

Where parameters c , c_1 and $V_{f,\max}$ depend on the type of array. For a hexagonal array, these parameters are given in [22].

At the channel-tows interface, the matching conditions are given by equations (7) to (10):

- *Continuity of normal velocities:*

$$u_i^{(s)} \hat{n}_i = u_i^{(d)} \hat{n}_i \quad (7)$$

- *Jump of tangential velocities:* this condition has been widely discussed in the literature [23, 24], but the most common is the slip condition of Beavers-Joseph that reads [25, 26]

$$\mu \left(\frac{\partial u_i}{\partial x_j} + \frac{\partial u_j}{\partial x_i} \right)^{(s)} \hat{n}_j \hat{\tau}_i = \frac{\gamma \mu}{\sqrt{\text{tr}(K)}/2} \left(u_i^{(d)} - u_i^{(s)} \right) \hat{\tau}_i \quad (8)$$

When the ratio between the height of the porous medium and the square root of permeability is very high, a good approximation for the slip coefficient, γ , is [27]:

$$\gamma = 1 / (\varepsilon_t^{1/2}) \quad (9)$$

A deeper discussion about the Beavers-Joseph condition for this application and its numerical treatment can be found in [21].

- *Continuity of surface tractions:*

$$\hat{n}_i \sigma_{ij}^{(s)} \hat{n}_j = -p^{(d)} \quad (10)$$

For the problem represented in Figure 1, the boundary conditions can be classified into three types:

- For the inlet and outlet of the channel domain, uniform horizontal tractions are considered, equations (11, 12):

$$t_1^{inl} = -\overline{p_{inl}} \cdot \hat{n}_1, u_2^{inl} = 0 \quad (11)$$

$$t_1^{out} = -\overline{p_{out}} \cdot \hat{n}_1, u_2^{out} = 0 \quad (12)$$

- No penetration conditions at the Darcy domains (tows) is given by equation (13):

$$\partial p / \partial \hat{n} = 0 \quad (13)$$

- Free-surface conditions at the liquid-air interfaces are stated in equations (14) to (16):

$$dx_i / dt = u_n \hat{n}_t = (u_j \cdot \hat{n}_j) \hat{n}_t \quad (14)$$

$$p - p_{air} = -p_{cap} \quad (15)$$

$$u_n = - [K_i / (\varepsilon_t \mu)] \cdot (\partial p / \partial x_i) \hat{n}_i \quad (16)$$

At the liquid-air interface corresponding to the bubble front when void migration occurs, capillary pressure is computed as $p_{cap} = -\sigma \kappa = -\sigma (\nabla \cdot \hat{n})$, where the curvature at the liquid-air interface, κ , is numerically computed as shown in [21, 28]. On the other hand, in the porous medium, the capillary pressure for the warps is calculated with equation (17) [29]:

$$p_{cap} = 2 (\lambda \cdot \cos(\theta) / R_{ec}) \quad (17)$$

Where the equivalent capillary radius, R_{ec} , is given by equation (18):

$$R_{ec} = 2 (A_{int,s} / C_{int,s}) (\varepsilon_t / (1 - \varepsilon_t)) \quad (18)$$

For $0 \leq \varphi < \pi/2$, equations for $A_{int,s}$ and $C_{int,s}$ are (19) and (20), respectively [21, 30]:

$$A_{int,s} = n_f \pi R_f^2 \sec(\varphi) \quad (19)$$

$$C_{int,s} = n_f \pi R_f (1 + \sec(\varphi)) \left(1 + \sum_{i=1}^{\infty} \left(\frac{1}{i} \right)^2 \left(\frac{\sec(\varphi) - 1}{\sec(\varphi) + 1} \right)^{2i} \right) \quad (20)$$

If the impregnation occurs perpendicular to the fibers ($\varphi = \pi/2$), equations (21) and (22) apply:

$$A_{int,s} = 2n_f L_f R_f \quad (21)$$

$$C_{int,s} \approx 2n_f L_f \quad (22)$$

For the wefts, capillary pressure is estimated as posed in equations (23)-(27) [31]:

$$p_{cap} = (\lambda/R_f) \cdot [\sin(\beta_{sup} + \theta) - \sin(\beta_{inf} + \theta)] / \left(\frac{5\pi}{6}(1 + \eta) - 1 - \sqrt{3}/2 \right) \quad (23)$$

$$\eta = d/R_f \quad (24)$$

$$\beta_{sup} \cong (\pi/2 - \theta) \quad (25)$$

$$\beta_{inf} \cong (\theta - \pi/2) \quad (26)$$

$$\eta = \sqrt{\pi / \left(2\sqrt{3}(1 - \varepsilon_t) \right)} - 1 \quad (27)$$

2.2 Integral equation formulations and numerical techniques

The numerical treatment of the governing equations, boundary conditions, and matching conditions of the Stokes-Darcy approach was adopted from [21]; the present section summarizes the main points of this treatment. The Boundary Element Method (BEM) is used here to solve the governing equations. The boundary integral formulations for the Stokes [32] and Darcy anisotropic [33–35] equations are given by (28) and (29), respectively:

$$c_{ij}(\xi) u_j(\xi) = \int_S K_{ij}(\xi, y) u_j(y) dS_y - \int_S U_i^j(\xi, y) t_j(y) dS_y \quad (28)$$

$$c(\xi^e) p(\xi^e) = \int_S p^*(\xi^e, y^e) q(y^e) dS_{y^e} - \int_S q^*(\xi^e, y^e) p(y^e) dS_{y^e} \quad (29)$$

where: $c_{ij} = (\alpha/2\pi)\delta_{ij}$, with α as the solid angle at the source point, whose value is $\alpha = \pi$ for points located over a smooth contour. For points located inside the domain, $c_{ij} = \delta_{ij}$. In a similar fashion, $c(\xi^e)$ is equal to 1/2 for points over a smooth surface and to 1, for points inside the domain. On the other hand, the superscript

“e” represents the Equivalent Isotropic System (EIS). The integral kernels in (28) and (29) are given in terms of the corresponding fundamental solutions equations (30 to (36):

$$U_i^j(\xi, y) = -\frac{1}{4\pi} \left[\ln\left(\frac{1}{r}\right) \delta_{ij} + \frac{(\xi_i - y_i)(\xi_j - y_j)}{r^2} \right] \quad (30)$$

$$K_{ij}(\xi, y) = -\frac{1}{\pi} \frac{(\xi_i - y_i)(\xi_j - y_j)(\xi_k - y_k) n_k(y)}{r^4} \quad (31)$$

$$p^*(\xi^e, y^e) = -\frac{1}{2\pi} \ln(r^e) \quad (32)$$

$$q^*(\xi^e, y^e) = -\frac{1}{2\pi(r^e)^2} \quad (33)$$

$$\left[(y_1^e - \xi_1^e) f^e \widehat{n}_1^e(y) + (y_2^e - \xi_2^e) f^e \widehat{n}_2^e(y) \right]$$

$$f^e = \left\| (K_1/K_2)^{1/4} \widehat{n}_1, (K_2/K_1)^{1/4} \widehat{n}_2 \right\| \quad (34)$$

$$r = |\xi - y| \quad (35)$$

$$r^e = |y^e - \xi^e| \quad (36)$$

where ξ (ξ^e in the EIS system) and y (y^e in the EIS system) are the source and field points, respectively, with the integrals containing the fundamental solutions $U_i^j(\xi, y)$ (Stokes) and $p^*(\xi^e, y^e)$ (Darcy) corresponding to the Single Layer Potential (SLP), and those ones containing $K_{ij}(\xi, y)$ (Stokes) and $p^*(\xi^e, y^e)$ (Darcy) to the Double Layer Potential (DLP). The factor f^e comes from the transformation of the normal vectors, as shown in [21].

The following characteristics of the numerical setup are deemed in the present work: second-order isoparametric discretization of the boundary and physical variables, non-continuous shape functions for the corner elements, numerical calculation of integrals using Gaussian quadrature, rigid body motion principle [34, 36] and Telles transformation [37] for the numerical treatment of strong and weak singularities, respectively. Details about the numerical treatment of the Beavers-Joseph condition, equation (8), are given in [21]. By imposing the boundary and matching conditions, a well-posed system of equations is obtained, which is solved using a Singular Value Decomposition (SVD) algorithm [38, 39].

Tracking of the free surfaces is done by implementing first-order Euler integration of equation (14). Time step selection according to physical, numerical and geometrical constraints, the implementation of remeshing and smoothing algorithms depending on the pressure and capillary forces, and the numerical calculation of surface curvatures, are critical issues for such tracking technique. This is thoroughly discussed in Appendix of [40].

The fluid velocity inside the channel is computed using (28) with $c_{ij} = \delta_{ij}$. The integral representation for the pressure is used to compute the pressure field inside the channel as shown in equation (37) [34]:

$$p(\xi) = 2\mu \int_S \Pi_{ik}(\xi, y) \widehat{n}_k(y) u_i(y) dS_y - \int_S p_i(\xi, y) t_i(y) dS_y \quad (37)$$

where $p_i(\xi, y) = -1/(2\pi r^2) \cdot (\xi_i - y_i)$ is the fundamental solution for the pressure equation, and $\Pi_{ik}(\xi, y) = \frac{1}{2\pi} [\delta_{ik}/r^2 - (2/r^4) \cdot (\xi_i - y_i)(\xi_k - y_k)]$ is the gradient of $p_i(\xi, y, y)$. The pressure field inside the tows is obtained from (29) with $c(\xi) = 1$, while the pressure gradient is found by taking the directional derivative of (29), as shown in equation (38):

$$\frac{\partial p(\xi^e)}{\partial \xi_i^e} = \int_S \frac{\partial p^*(\xi^e, y^e)}{\partial \xi_i^e} q(y^e) dS_{y^e} - \int_S \frac{\partial q^*(\xi^e, y^e)}{\partial \xi_i^e} p(y^e) dS_{y^e} \quad (38)$$

The velocities in the interior points of the porous media are given by the Darcy's law, in terms of the pressure gradient, equation (38).

3. Results and discussion

3.1 Validation of the BEM method for Stokes-Darcy problems

To verify the developed BEM code, the coupled Stokes-Darcy problem of Figure 2 that admits an analytical solution is considered. In this problem, botgh the free-fluid (Stokes) and porous medium (Darcy) sub-domains are totally saturated. For the porous medium, porosity is set to $\varepsilon_t = 0.6$, leading to a slip coefficient of $\gamma = 1.29$ according to equation 9. For this particular problem, an analytical solution for the pressure and velocity field in terms of power series was developed in [21], which is reproduced in the following equations(39) to [52] For the anisotropic porous medium ($0 \leq y \leq h_d$)

$$p = a_o (K_2/K_1)^{\frac{1}{4}} x + b_o + \sum_{n=1}^{\infty} a_n \cdot \cosh \left(\lambda_n \cdot (K_1/K_2)^{\frac{1}{4}} (h_d - y) \right) \cdot \sin \left(\lambda_n \cdot (K_2/K_1)^{\frac{1}{4}} x \right) \quad (39)$$

$$a_o = (p_{cap} - p_{in}) / l^e \quad (40)$$

$$b_o = p_{in} \quad (41)$$

$$\lambda_n = (n\pi) / l^e \quad (42)$$

$$l^e = (K_2/K_1)^{1/4} l \quad (43)$$

$$u_x = -\frac{K_1}{\mu} \cdot \left(\frac{dp}{dx} \right) \quad (44)$$

$$u_y = -\frac{K_2}{\mu} \cdot \left(\frac{dp}{dy} \right) \quad (45)$$

For the channel domain ($-h_s \leq y \leq 0$):

$$p = p_{in} - (p_{in}/l) x + \sum_{n=1}^{\infty} a_n \cdot M_n \cdot \sin \left(\lambda_n \cdot (K_2/K_1)^{1/4} x \right) \quad (46)$$

$$M_n = -\frac{1}{A_1} \cdot \left[h_s \frac{K_1}{\mu} \cosh \left(\lambda_n \cdot (K_1/K_2)^{1/4} h_d \right) + \frac{K_2}{\mu} \left(\frac{(K_1/K_2)^{3/4}}{\lambda_n} \right) \sinh \left(\lambda_n \cdot (K_1/K_2)^{1/4} (h_d) \right) \right] \quad (47)$$

$$A_1 = h_s^3 / (3\mu) + \sqrt{K_1 + K_2} \cdot h_s^2 / (\mu\gamma\sqrt{2}) \quad (48)$$

$$u_x = \frac{1}{2\mu} \cdot \left(\frac{dp}{dx} \right) \cdot (y^2 + 2h_s y) + u_1^-(x) \quad (49)$$

$$u_y = -\frac{1}{2\mu} \cdot \left(\frac{d^2 p}{dx^2} \right) \cdot \left(\frac{y^3}{3} + h_s y^2 - \frac{2}{3} h_s^3 \right) - \left(\frac{du_1^-}{dx_1} \right) (y + h_s) \quad (50)$$

$$a_n = -2l \left(a_o (K_2/K_1)^{1/4} - c_o \right) / (n\pi F_n) (-1)^n \quad (51)$$

The Fourier coefficients of (39) and (46) are given by:

$$F_n = M_n \left(1 + \frac{2\sqrt{K_1 + K_2}}{\gamma\sqrt{2}} h_s \cdot \lambda_n^2 \cdot (K_2/K_1)^{1/2} \right) - \cosh \left(\lambda_n \cdot (K_1/K_2)^{\frac{1}{4}} \cdot h_d \right) \left(1 - 2K_1 \lambda_n^2 \cdot (K_2/K_1)^{\frac{1}{2}} \right) \quad (52)$$

The L^2 relative error norms between the analytical and

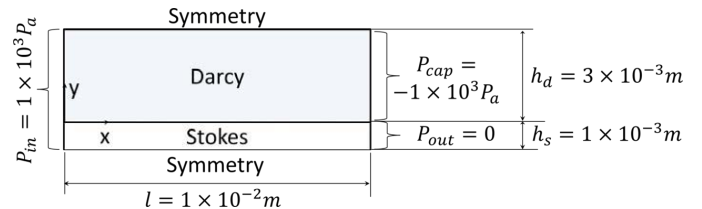


Figure 2 Scheme and boundary conditions of coupled Stokes-Darcy problem

the BEM solutions for the pressure, p , and velocities, u_x

and u_y , are shown in Table 1. Three factors are considered for the analysis of these errors: mesh size [h], anisotropic ratio [K_1K_2] and slip coefficient [γ]. The mesh size is reported as $h = e/H$, where $H = h_d + h_s$ is the total height of the domain [See Figure 2] and e represents the element size. According to Table 1, the maximum error for a determined mesh size is always obtained for the horizontal velocity, u_x , when $K_1K_2 = 0.1$ and $\gamma = 0.01$, but this error decreases as the mesh is finer. In general, the refinement of the mesh leads to the reduction of the L^2 error in all situations, which means that the BEM code converges to the analytical solution; however, the order of convergence is not necessarily the same in all cases. The vertical velocities, u_y , are not considered in the present analysis since they are very close to zero; however, as observed in Table 1, the accuracy corresponding to u_y is acceptable enough in all situations.

The slip coefficients of coupled Stokes-Darcy simulations of the following sections are calculated using the equation (9) and have an order of magnitude of $\mathcal{O}(0)$. Considering the results achieved for $\gamma = 1.29$ in the Table 1, it is expected to obtain an acceptable accuracy for those simulations, even for the coarser mesh evaluated here, i.e., $h = 1 \times 10^{-1}$. In order to define the suitable mesh size for simulations of the following sections, both the L^2 relative error norms and the run times are deemed. The CPU times obtained with an Intel Pentium 2.1 GHz and 2GB of memory are shown in Figure 3. Let us consider the change of mesh size from $h = 1 \times 10^{-1}$ to $h = 5 \times 10^{-2}$, where average reductions of the L^2 relative error norm of 33.7% and 32.3% are obtained for pressure and horizontal velocity, respectively, leading to an increment in the CPU time of 6.49 times; in such case, mesh refinement could be considered appropriate. On the other hand, when mesh-size changes from $h = 1 \times 10^{-1}$ to $h = 3.3 \times 10^{-2}$, the increment of the CPU time is 23.40 times, while error reduces by 48.2% for the pressure and 54.3% for the horizontal velocity, which can be considered impractical in this case. Taking this in mind, the mesh-size is taken as $h = 5 \times 10^{-2}$ in the following simulations.

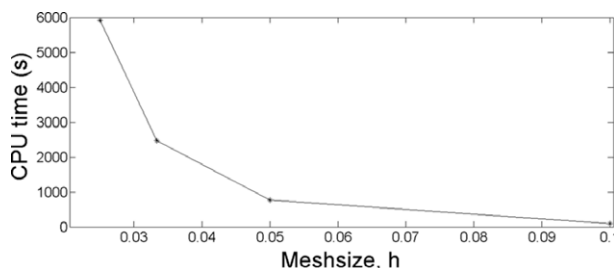


Figure 3 Run time vs. Mesh-size for the coupled problem

3.2 Comparison between the present Stokes-Darcy approach and the classical approach

The main differences between the classical approach, where the channel flow is not modeled and a uniform pressure is supposed in the channel, and the present approach, where the channel flow is modeled by the Stokes equation and it is prescribed a pressure gradient, can be noticed when comparing simulations of Figures 4a to 4c and 5a to 5k. For each filling instant, the time normalized with the total time of simulation (t/t_{sim}), warps saturation (S_{warps}), weft saturation (S_{weft}) and total tows saturation (S_t) are shown; the x and y coordinates are non-dimensionalized as $x^* = x/L_{RUC}$ and $y^* = y/L_{RUC}$. The geometric and material inputs of both simulations are shown in Table ??, where it is also observed that for the simulation with the classical approach (Figures 4a to 4c) a uniform channel pressure of $\langle P_g \rangle^g = 122\text{kPa}$ is prescribed, while for the simulation with the present approach (Figures 5a, to 5k), inlet and outlet pressures of $p_{in} = 125.5\text{kPa}$ and $p_{out} = 118.5\text{kPa}$ are considered, which originates a pressure gradient along the RUC of $\Delta P/\Delta x = 5.83 \times 10^3\text{kPa/m}$, with an average pressure of $\langle P_g \rangle^g = 122\text{kPa}$, agreeing with the average pressure of the other approach. For simulation of Figures 4a to 4c, constant atmospheric pressure is considered for the air given the full air dissolution assumption; on the other hand, in the current approach, Figures 5a to 5k, a vacuum pressure of $P_{vac} = -75\text{kPa}$ is deemed, varying in the weft following the ideal gas law.

For the classical approach, as observed in Figures 4a to 4c, the fluid flow motion in warps and weft is uniform, namely, towards the edges and the center of the RUC; this occurs because the pressure is the same at the channel-tows interface. Total saturation is possible with this approach (Figure 4c), with the complete filling of warps happening first (Figure 4b). Thus, according to this approach, full air dissolution is possible. However, this is ideal case does not necessarily correspond to a real application.

On the other hand, for the present Stokes-Darcy approach, considering full air compression in the weft, three stages can be clearly identified for the void in Figure 5a to 5k compression, mobilization and migration. In the compression stage, the fluid fronts in the warps are not parallel to inferior and superior edges of the RUC, and the fluid front in weft is barely decentered (see datatips in Figure 5a), which is caused by the imposition of a pressure gradient along the flow direction in the channel; this phenomenon is more perceptible for greater pressure gradients. The filling of the warps occurs at 2.7% of the total simulation time (Figure 5b). When the equilibrium condition is achieved for the trapped

Table 1 Evaluation of the accuracy of the BEM code for the coupled problem L^2 relative error norms are reported by 10^{-2}

		L^2 relative error norms											
Mesh size(h)	Variable	$K_1/K_2 = 0.1$			$K_1/K_2 = 1$			$K_1/K_2 = 10$			$K_1/K_2 = 100$		
		$\gamma =$	$\gamma =$	$\gamma =$	$\gamma =$	$\gamma =$	$\gamma =$	$\gamma =$	$\gamma =$	$\gamma =$	$\gamma =$	$\gamma =$	
1, 00	p	1.29	0.1	0.01	1.29	0.1	0.01	1.29	0.1	0.01	1.29	0.1	0.01
	u_x	4.93	4.91	4.90	4.78	4.78	4.77	5.04	5.04	5.03	5.70	5.70	5.70
	$E - 01$	u_y	1.64	9.46	17.7	1.04	5.12	14.9	0.96	4.01	13.6	0.95	3.87
5, 00	p	4.22	4.11	3.95	4.79	4.81	4.98	4.94	4.97	5.42	5.10	5.18	6.28
	u_x	3.11	3.11	3.10	3.07	3.07	3.07	3.33	3.34	3.34	4.24	4.24	4.24
	$E - 02$	u_y	1.15	6.85	12.6	0.65	3.72	10.7	0.56	2.91	9.76	0.56	2.81
3, 33	p	4.20	4.09	3.95	4.77	4.79	4.92	4.92	4.92	4.96	5.02	5.03	5.27
	u_x	2.43	2.42	2.43	2.38	2.38	2.39	2.61	2.61	2.61	3.37	3.37	3.37
	$E - 02$	u_y	0.98	5.96	10.9	0.52	3.24	9.26	0.43	2.54	8.48	0.43	2.45
2, 50	p	4.16	4.02	3.78	4.73	4.72	4.71	4.91	4.91	4.93	4.99	5.00	5.09
	u_x	2.01	2.00	2.00	1.96	1.97	1.97	2.18	2.19	2.19	2.97	2.97	2.97
	$E - 02$	u_y	0.84	5.11	9.30	0.44	2.78	7.91	0.36	2.18	7.25	0.37	2.10

Table 2 Simulations data for BEM simulations with both approaches

Geometric and material data common for both simulation												
H_{RUC}	L_{RUC}	H_g	a_1	a_1	μ	K_1	K_2	λ	θ	R_f	ε_t	μ_{air}
(m)	(m)	(m)	(m)	(m)	(Pa.s)	(m^2)	(m^2)	(mN/m)		(μm)		(Pa.s)
4.50	1.20	3.00	5.00	1.00	0.1	2.07	1.08	15	30°	9.96	0.19	18.6
E-04	E-03	E-04	E-04	E-04		E-13	E-14					E-06
Numerical parameters												
Anisotropic ratio, K_1/K_2				Slip coefficient, γ				Relative mesh-size, h				
19.17				1.29				5×10^{-2}				
Processing data												
Classical approach			Present Stokes-Darcy approach									
$\langle P_g \rangle^g$ (kPa)			p_{in} (kPa)	p_{out} (kPa)	$\Delta P/\Delta x$ (kPa/m)			$\langle P_g \rangle^g$ (kPa)		P_{vac} (kPa)		
122			125.5	118.5	5.83×10^3			122		-75		

Note: In this table, H_{RUC} , L_{RUC} , H_g , a_1 , a_2 , μ , K_1 , K_2 , λ , θ , R_f , ε_t and μ_{air} stand for the height of the RUC, length of the RUC, height of the channel or gap, major axis of the weft, minor axis of the weft, liquid viscosity, major permeability, minor permeability, surface tension, contact angle, fiber radius, tow porosity and air viscosity, respectively.

bubble, air compression ceases, and void mobilization starts (green line in Figure 5c). From this time instant until the onset of void migration, weft saturation, S_{weft} , is essentially constant, reaching an equilibrium saturation where void shifts towards the right extreme of the weft at constant volume (Figures 5d to 5g). Small changes of S_{weft} during this process of void displacement can be present by numerical errors during the fluid front tracking, but they can be neglected. The compression phenomenon lasts 13.3% of the total simulation time, whereas the void mobilization takes almost the remaining time, namely, 86.7%. When the void reaches the right extreme of weft, Figure 5f, normalized time is $t/t_{sim} = 1 - 2.80 \times 10^{-5}$, which is very close to one because the time elapsed from this instant until the end of the simulation (the time of partial migration of the bubble), is much shorter than the times corresponding to void compression and void

mobilization. The process of void migration can be seen in Figures 5h to 5k. The balance between capillary forces, which depend on the surface tension (λ) and on the curvature of the bubble surface (κ), and pressure forces of the compressed air, which changes with the bubble expansion or shrinking, determines the dynamic evolution of the intra-tow void.

3.3 Velocity field and streamlines

In Figures 6a to 6c, the velocity fields and streamlines when the bubble is compressing inside the weft and the warps are totally saturated are shown; that is, there is no mass transfer from the channels into the warps; some figures are off-scale for visualization purposes. Several features can be identified in Figures 6a to 6c for the channel domain. Firstly, the velocity vectors

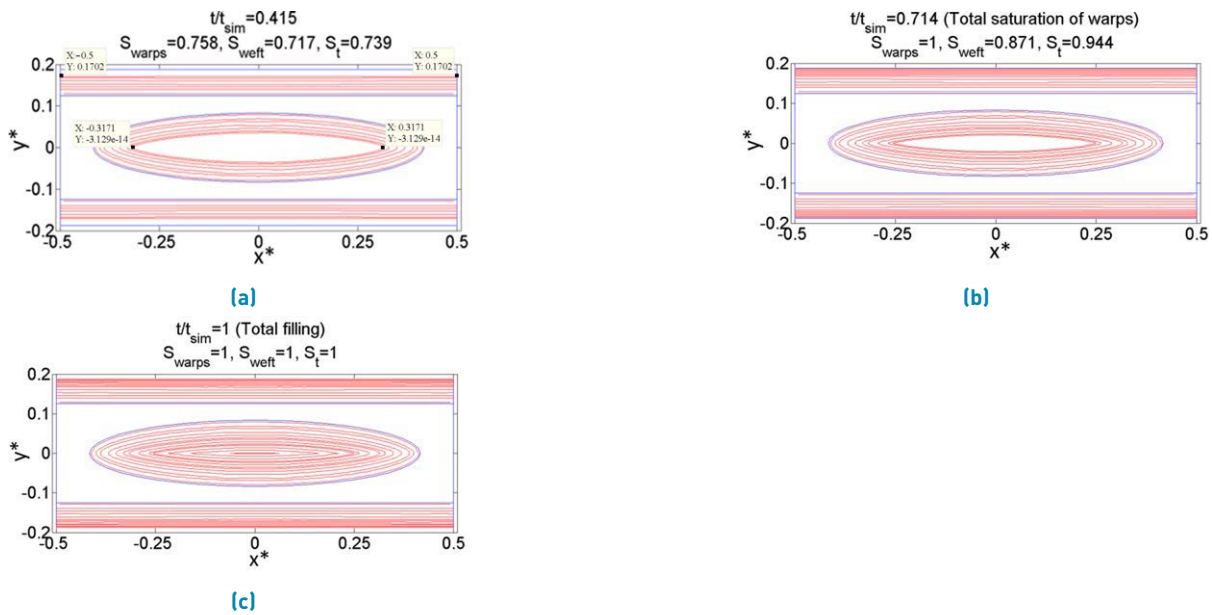


Figure 4 Filling instants with the traditional approach. a) Warps and weft are partially filled, b) Warps are fully saturated, c) RUC is totally saturated

at the interface with the weft are almost tangential to such interface (Figures 6b and 6c), which means that the magnitude of the normal penetration velocity into the weft is very small in comparison with the tangential velocity. It is also remarkable the increment in the magnitude of the velocity with the reduction of the inter-tow space (Figures 6a to 6c) because this indicates that the effect of this reduction in the velocity field is more relevant than the effect of the liquid absorption into the tows that reduces the velocity magnitude along the RUC. Regarding the streamlines, the BEM code predicts that the inferior ones (nearby to the lower edge of Figures 6a) tend to concentrate at the symmetric boundary as the inter-tow space reduces. In general, when a streamline traverses the whole RUC, it ends at a lower vertical position with respect to its starting vertical position and this is more notorious as the streamlines are closer to the symmetric boundary.

On the other hand, for the weft domain (Figure 6d to 6h), it can be appreciated that the velocity at the channel-weft interface is essentially normal to such interface; this means that the tangential Darcy velocity appearing in equation (8), $u_i^{(d)} \hat{t}_i$, is negligible. It is also worth noting, by comparing the magnitudes of the velocity vectors along the channel-weft interface (Figure 6d), that the mass transfer is greater as the inter-tow space is lower, in such a way that the normal velocities at the channel-weft interface are larger in points close to the center of the weft, whereas they are smaller in the neighborhoods of the right and left edges of the weft. The mass transfer in the left half of the weft is barely greater than the mass transfer in

the right half, but this difference is enough to generate a decentered bubble, as it was shown in Figure 5a. As it can be appreciated in Figure 6h, most of the streamlines with positions of starting points beyond the horizontal limits defined by the fluid front, converge in the right and left extremes of such a fluid front, and the starting points of these streamlines coincide with the points of low mass transfer, as it can be noticed by comparing Figures 6d and 6h.

The velocity fields and streamlines when the bubble migration occurs are represented in Figures 7a to 7g. For the channel domain (Figures 7a, 7b), it can be appreciated that the highest velocities are obtained in the region of bubble migration, which means that the average air migration velocity, $\langle u_{air} \rangle$, is greater than the average liquid velocity in the channel, $\langle u_g \rangle^g$, for this particular case. As observed in Figure 7a, the streamlines starting in the inlet boundary encounter with those ones starting in the contour of the partially escaped bubble and this causes the accumulation of the former ones in the right inferior zone of the RUC. In Figures 7a, likewise to the formerly commented case of void compression in the weft (Figures 6a), a high density of streamlines can be observed in the symmetric boundary of the RUC when the inter-tow distance is the smallest, namely, in the half of the RUC. For the weft domain (Figures 7c to 7f), the velocity magnitudes are larger in points whose horizontal position is between the horizontal limits defined by the fluid front, as in the last case analyzed (Figures 6d, 6f 6g). In this case, most of the streamlines starting in the zone of low mass transfer, where the normal interfacial velocities are smaller, converge in the left extreme of the

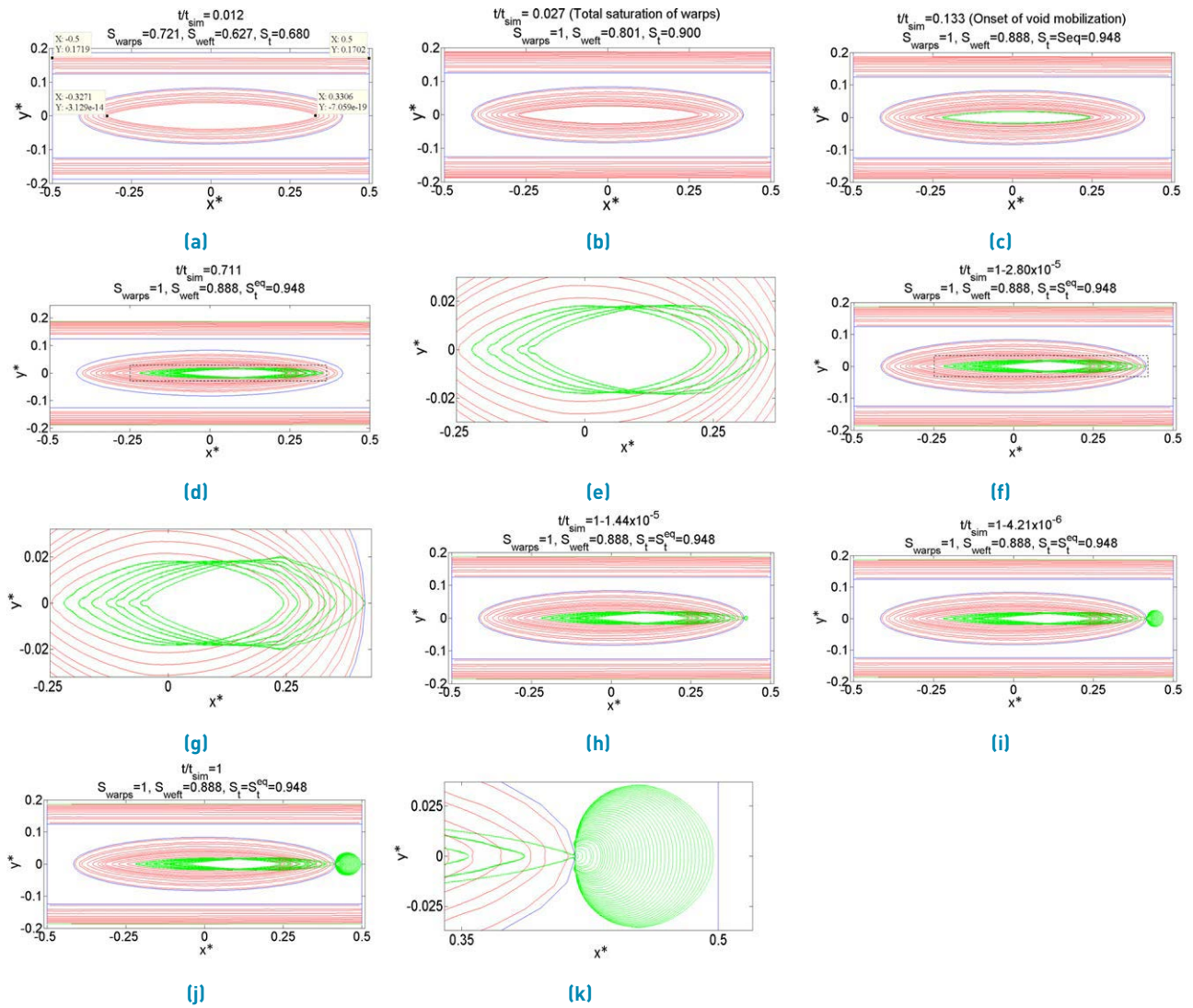


Figure 5 of filling with the Stokes-Darcy approach considering full air compressibility. a) Warps and weft partially filled, b) Warps totally saturated, c) Void compression finishes and void mobilization begins, d) Void moves towards the right extreme of the weft, e) Detail of Figure 5d, f) Void arrives at the right extreme of weft and void migration starts, g) Detail of Figure 5f, h) Stage 1 of void migration, i) Stage 2 of void migration, j) Stage 3 of void migration, k) Detail of void migration

fluid front (See Figures 7c). According to Figure 7g, in the right extreme of the weft, some streamlines are very short since the interface channel-weft, where the streamlines start, is adjacent to the fluid front, where the streamlines finish.

4. Conclusions

In the present work, a new approach to conducting filling simulations of dual-scale fibrous reinforcements at a mesoscopic scale was presented. According to the numerical results, this approach allows capturing several phenomena involved during the dynamic evolution of intra-tow voids generated in these reinforcements:

compression, mobilization at constant volume, and migration from tows toward the channel. BEM results show that the former two phenomena (compression and mobilization) have a timescale of several orders of magnitude larger than the timescale of the bubble migration; additionally, the BEM code predicts that the process of void mobilization inside the tow takes more time than the void compression.

The analysis of the velocity field and streamlines allows concluding that, at the interface channel-weft, the tangential Darcy velocity is negligible, and the mass transfer from the channel towards the weft is not uniform, being greater in points whose horizontal position is between the horizontal limits defined by the fluid front

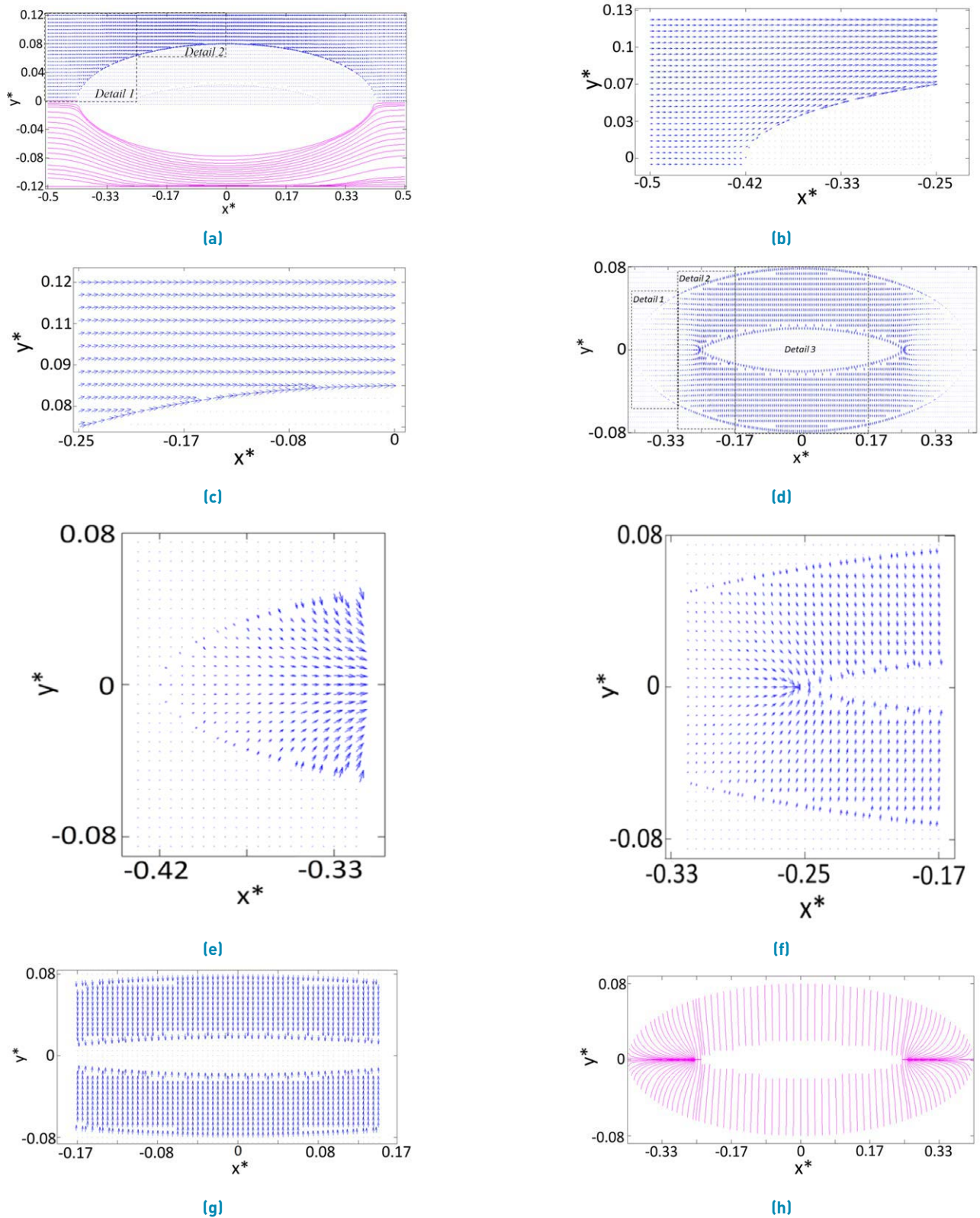


Figure 6 Velocity field and streamlines when the bubble is compressing. a) Velocity field and streamlines for the channel domain, b) Detail 1 of Figure 6a, c) Detail 2 of Figure 6a, d) Velocity field for the weft domain, e) Detail 1 of Figure 6d, f) Detail 2 of Figure 6d, g) Detail 3 of Figure 6d, h) Streamlines for the weft domain

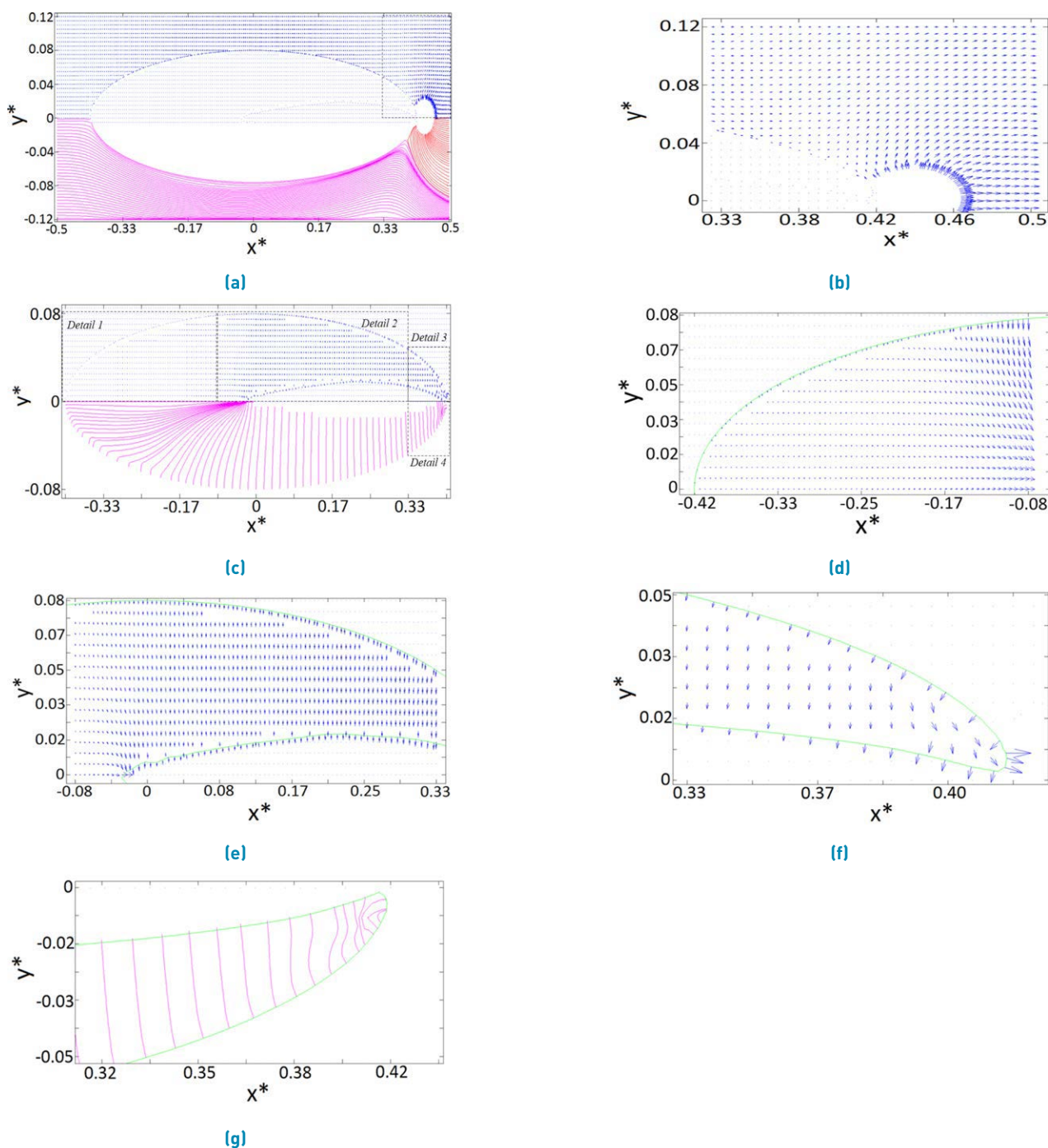


Figure 7 Velocity field and streamlines when the bubble is partially escaping. a) Velocity field and streamlines for the channel domain, b) Detail of Figure 7a, c) Velocity field and streamlines for the weft domain, d) Detail 1 of Figure 7c, e) Detail 2 of Figure 7c, f) Detail 3 of Figure 7c, g) Detail 4 of Figure 7c

inside the tows, and considerably decreasing in points with horizontal positions beyond these limits. The streamlines corresponding to the zones of low mass transfer tend to converge in the horizontal extremes of the fluid front.

5. Declaration of competing interest

I declare that I have no significant competing interests, including financial or non-financial, professional, or personal interests interfering with the full and objective presentation of the work described in this manuscript.

6. Acknowledgements

The autor of the present work acknowledge the financial support of Institución Universitaria Pascual Bravo for the development of the research project “Diseño de estrategias de inyección asistido por simulación computacional para reducir la formación de vacíos y mejorar el desempeño mecánico de piezas fabricadas por procesos de moldeo líquido”, which supports the present work.

7. Funding

This work was financially supported by Institución Universitaria Pascual Bravo.

8. Author contributions

Iván David Patiño: Development of computational model, results analysis and conclusions, writing of the manuscript.

9. Data availability statement

The author confirms that the data supporting the findings of this study are available within the article or its supplementary materials.

References

- [1] H. Jinlian, L. Yi, and S. Xueming, “Study on void formation in multi-layer woven fabrics,” *Composites Part A: Applied Science and Manufacturing*, vol. 35, no. 5, May, 2004. [Online]. Available: <https://doi.org/10.1016/j.compositesa.2003.11.007>
- [2] D. H. Lee, W. I. Lee, and M. K. Kang, “Analysis and minimization of void formation during resin transfer molding process,” *Composites Science and Technology*, vol. 66, no. 16, Dec. 18, 2006. [Online]. Available: <https://doi.org/10.1016/j.compscitech.2005.07.008>
- [3] B. Gourichon, C. Binetruy, and P. Krawczak, “A new numerical procedure to predict dynamic void content in liquid composite molding,” *Composites Part A: Applied Science and Manufacturing*, vol. 37, no. 11, Nov., 2006. [Online]. Available: <https://doi.org/10.1016/j.compositesa.2005.12.017>
- [4] K. M. Pillai, “Governing equations for unsaturated flow through woven fiber mats. part 1. isothermal flows,” *Composites Part A: Applied Science and Manufacturing*, vol. 33, no. 7, Jul. 1, 2002. [Online]. Available: [https://doi.org/10.1016/S1359-835X\(02\)00034-9](https://doi.org/10.1016/S1359-835X(02)00034-9)
- [5] K. M. Pillai and M. S. Munagavalasa, “Governing equations for unsaturated flow through woven fiber mats. part 2. non-isothermal reactive flows,” *Composites Part A: Applied Science and Manufacturing*, vol. 35, no. 4, Apr. 2004. [Online]. Available: <https://doi.org/10.1016/j.compositesa.2004.01.001>
- [6] H. Tan and K. M. Pillai, “Multiscale modeling of unsaturated flow of dual-scale fiber preform in liquid composite molding ii: Non-isothermal flows,” *Composites Part A: Applied Science and Manufacturing*, vol. 43, no. 1, Jan. 2012. [Online]. Available: <https://doi.org/10.1016/j.compositesa.2011.06.012>
- [7] M. S. Munagavalasa and K. M. Pillai, “An estimation of effective thermal conductivity of a fibrous dual-scale porous medium during unsaturated flow,” *International Journal of Heat and Mass Transfer*, vol. 49, no. 1-2, Jan. 2006. [Online]. Available: <https://doi.org/10.1016/j.ijheatmasstransfer.2005.06.020>
- [8] M. S. Munagavalasa, “Theoretical modeling of unsaturated flow in fibrous dual-scale porous media using the volume averaging method,” Ph.D. thesis, Dissertation, College Of Engineering and Applied Science, University of Wisconsin Milwaukee, USA, 2006.
- [9] J. M. Lawrence, V. Neacsu, and S. G. Advani, “Modeling the impact of capillary pressure and air entrapment on fiber tow saturation during resin infusion in LCM,” *Composites Part A: Applied Science and Manufacturing*, vol. 40, no. 8, Aug. 2009. [Online]. Available: <https://doi.org/10.1016/j.compositesa.2009.04.013>
- [10] H. Tan, “Simulation of flow in dual-scale porous media,” Ph.D. thesis, Dissertation, College Of Engineering and Applied Science, University of Wisconsin Milwaukee, USA, 2011.
- [11] P. Simacek and S. G. Advani, “A numerical model to predict fiber tow saturation during liquid composite molding,” *Composites Science and Technology*, vol. 63, no. 12, Sep. 2003. [Online]. Available: [https://doi.org/10.1016/S0266-3538\(03\)00155-6](https://doi.org/10.1016/S0266-3538(03)00155-6)
- [12] H. Tan and K. M. Pillai, “Multiscale modeling of unsaturated flow in dual-scale fiber preforms of liquid composite molding i: Isothermal flows,” *Composites Part A: Applied Science and Manufacturing*, vol. 43, no. 1, Jan. 2012. [Online]. Available: <https://doi.org/10.1016/j.compositesa.2010.12.013>
- [13] P. Simacek and S. G. Advani, “Modeling resin flow and fiber tow saturation induced by distribution media collapse in vartm,” *Composites Science and Technology*, vol. 67, no. 13, Oct. 2007. [Online]. Available: <https://doi.org/10.1016/j.compscitech.2007.02.008>
- [14] Y. Wang and S. M. Grove, “Modelling microscopic flow in woven fabric reinforcements and its application in dual-scale resin infusion modelling,” *Composites Part A: Applied Science and Manufacturing*, vol. 39, no. 5, May. 2008. [Online]. Available: <https://doi.org/10.1016/j.compositesa.2008.01.014>
- [15] H. Tan and K. M. Pillai, “Modeling Unsaturated Flow in Dual-Scale Fiber Mats of Liquid Composite Molding: Some Recent Developments,” in *10th International Conference on Flow Processes in Composite Materials (FPCM10)*, Monte Verità, 2010.
- [16] F. Zhou, N. Kuentzer, P. Simacek, S. G. Advani, and S. Walsh, “Analytic characterization of the permeability of dual-scale fibrous porous media,” *Composites Science and Technology*, vol. 66, no. 15, Dec. 1, 2006. [Online]. Available: <https://doi.org/10.1016/j.compscitech.2006.02.025>
- [17] J. A. F. Zhou and S. G. Advani, “A closed form solution for flow in dual scale fibrous porous media under constant injection pressure conditions,” *Composites Science and Technology*, vol. 68, no. 3-4, Mar. 2018. [Online]. Available: <https://doi.org/10.1016/j.compscitech.2007.09.010>
- [18] L. He, S. Yan, Y. Li, P. Wen, X. Xie, and *et al.*, “Simulation of stochastic flow considering mesoscale permeability variability during the resin transfer molding process,” *Polym. Compos*, vol. 41, no. 5, May. 2020. [Online]. Available: <https://doi.org/10.1002/pc.25490>
- [19] P. Carlone, F. Rubino, V. Paradiso, and F. Tucci, “Multi-scale modeling and online monitoring of resin flow through dual-scale textiles in liquid composite molding processes,” *The International Journal of Advanced Manufacturing Technology*, vol. 96, no. 5, Feb. 21, 2018. [Online]. Available: <https://doi.org/10.1007/s00170-018-1703-9>
- [20] M. Imbert, S. Comas-cardona, E. Abisset-chavanne, and D. Prono, “Introduction of intra-tow release/storage mechanisms in reactive dual-scale flow numerical simulations,” *Journal of Composite Materials*, vol. 53, no. 1, 2019. [Online]. Available: <https://doi.org/10.1177/0021998318780498>
- [21] I. D. P. Arcila, H. Power, C. N. Londoño, and W. F. F. Escobar, “Boundary element simulation of void formation in fibrous reinforcements based on the stokes-darcy formulation,” *Computer Methods in Applied Mechanics and Engineering*, vol. 401, Jun. 1, 2016. [Online]. Available: <https://doi.org/10.1016/j.cma.2016.02.010>

- [22] B. R. Gebart, "Permeability of unidirectional reinforcements for rtm," *Journal of Composite Materials*, vol. 26, no. 8, Aug. 1, 1992. [Online]. Available: <https://doi.org/10.1177/002199839202600802>
- [23] A. Mikelic, W. Jäger, and W. J. Ager, "On the interface boundary condition of beavers, joseph, and saffman," *SIAM Journal on Applied Mathematics*, vol. 60, no. 4, 2000. [Online]. Available: <https://doi.org/10.1137/S003613999833678X>
- [24] M. L. Bars and M. G. Worster, "Interfacial conditions between a pure fluid and a porous medium: implications for binary alloy solidification," *Journal of Fluid Mechanics*, vol. 550, Mar. 10, 2006. [Online]. Available: <https://doi.org/10.1017/S0022112005007998>
- [25] Y. Cao, M. Gunzburger, F. Hua, and X. Wang, "Coupled stokes-darcy model with beavers-joseph interface boundary condition," *COMMUN. MATH. SCI.*, vol. 8, no. 1, 2010. [Online]. Available: <https://bit.ly/3KbTfW1>
- [26] G. S. Beavers, E. M. Sparrow, and R. A. Magnuson, "Experiments on coupled parallel flows in a channel and a bounding porous medium," *Journal of Basic Engineering*, vol. 92, no. 4, Dec. 15, 1970. [Online]. Available: <https://doi.org/10.1115/1.3425155>
- [27] L.-H. Huang, I.-L. Chiang, and C.-H. Song, "A re-investigation of laminar channel flow passing over porous bed," *Journal of the Chinese Institute of Engineers*, vol. 20, no. 4, Mar. 10, 1997. [Online]. Available: <https://doi.org/10.1080/02533839.1997.9741848>
- [28] I. D. Patiño, H. Power, C. Nieto-Londoño, and W. F. Flórez, "Stokes-Brinkman formulation for prediction of void formation in dual-scale fibrous reinforcements: a BEM/DR-BEM simulation," *Computational Mechanics*, vol. 59, no. 4, Feb. 16, 2017. [Online]. Available: <https://doi.org/10.1007/s00466-016-1360-5>
- [29] R. Masoodi and K. M. Pillai, "A general formula for capillary suction-pressure in porous media," *Journal of Porous Media*, vol. 15, no. 8, 2012. [Online]. Available: <https://doi.org/10.1615/JPorMedia.v15.i8.60>
- [30] T. Chandrupatla and T. Osler, "The perimeter of an ellipse," *Mathematical Scientist*, vol. 35, no. 2, Dec. 2010. [Online]. Available: <https://bit.ly/3k6Lo0L>
- [31] V. Neacsu, A. A. Obaid, and S. G. Advani, "Spontaneous radial capillary impregnation across a bank of aligned micro-cylinders – part i: Theory and model development," *International Journal of Multiphase Flow*, vol. 32, no. 6, Jun. 2006. [Online]. Available: <https://doi.org/10.1016/j.ijmultiphaseflow.2006.02.006>
- [32] O. A. Ladyzhenskaya, *The Mathematical Theory of Viscous Incompressible Flow*. New York: Gordon and Breach, 1963.
- [33] R. Gantois, A. Cantarel, G. Dusserre, J. N. Félices, and F. Schmidt, "Mold Filling Simulation of Resin Transfer Molding Combining BEM and Level Set Method," *Applied Mechanics and Materials*, vol. 62, Jun. 2011. [Online]. Available: <https://doi.org/10.4028/www.scientific.net/AMM.62.57>
- [34] C. Psirkidis, *A Practical Guide to Boundary Element Methods with the Software Library BEMLIB*. London: CRC Press, 2002.
- [35] D. L. Clements, *Boundary value problems governed by second order elliptic systems*. Boston: Pitman Advanced Pub. Program, 1981.
- [36] H. Power and L. C. Wrobel, *Boundary integral methods in fluid mechanics*. Southampton, UK ; Boston: Computational Mechanics Publications, 1995.
- [37] J. F. Telles, "A self-adaptive co-ordinate transformation for efficient numerical evaluation of general boundary element integrals," *International Journal for Numerical Methods in Engineering*, vol. 24, no. 5, May. 1987. [Online]. Available: <https://doi.org/10.1002/nme.1620240509>
- [38] A. Neumaier, "Solving ill-conditioned and singular linear systems: A tutorial on regularization," *SIAM Review*, vol. 40, no. 3, 1998. [Online]. Available: <https://doi.org/10.1137/S0036144597321909>
- [39] A. Rap, L. Elliott, D. B. Ingham, D. Lesnic, and X. Wen, "DRBEM for Cauchy convection-diffusion problems with variable coefficients," *Engineering Analysis with Boundary Elements*, vol. 28, no. 11, Nov. 2004. [Online]. Available: <https://doi.org/10.1016/j.enganabound.2004.06.003>
- [40] I. Patiño, H. Power, C. Nieto, and W. Flórez, "Boundary element method for the dynamic evolution of intra-tow voids in dual-scale fibrous reinforcements using a stokes-darcy formulation," *Engineering Analysis with Boundary Elements*, vol. 87, Feb. 2018. [Online]. Available: <https://doi.org/10.1016/j.enganabound.2017.11.014>